In vivo dual-scale photoacoustic surveillance and assessment of burn healing

ZHIYOU WU, FEI DUAN, JINDE ZHANG, SHI LI, HAOSONG MA, AND LIMING NIE[*]

State Key Laboratory of Molecular Vaccinology and Molecular Diagnostics & Center for Molecular Imaging and Translational Medicine, School of Public Health, Xiamen University, Xiamen 361102, China

[*]nielm@xmu.edu.cn

Abstract: Accurate diagnoses of superficial and deep dermal burns are difficult to make even by experienced investigators due to slight differences in dermis damage. Many imaging technologies have been developed to improve the burn depth assessment. But these imaging tools have limitations in deep imaging or resolving ability. Photoacoustic imaging is a hybrid modality combining optical and ultrasound imaging that remains high resolution in deep imaging depth. In this work, we used dual-scale photoacoustic imaging to noninvasively diagnose burn injury and monitor the burn healing. Real-time PACT provided cross-sectional and volumetric images of the burn region. High-resolution PAM allowed for imaging of angiogenesis on the hyperemic ring. A long-term surveillance was also performed to assess the difference between the two damage degrees of burn injuries. Our proposed method suggests an effective tool to diagnose and monitor burn injury.

1. Introduction

Burns are easily caused under thermal, electrical, chemical and radioactive threats. There are more than 486,000 burn injuries receiving medical intervention per year in the United States, estimated by the American Burn Association (ABA). Approximately 40,000 of these injuries require hospitalization and 3,275 die annually [1]. Severe skin burn injury can lead to not only local tissue damage but multiple organ dysfunction syndromes, which urgently demand accurate diagnosis for early burn treatment.

Clinical evaluation of burn depends on two important factors: the depth and area of burn injury. In term of depth, burns are categorized into epidermal burn, superficial dermal burn (SDB), deep dermal burn (DDB) and deep burn (DB) [2]. Epidermal burn and SDB, as superficial partial burns, can heal spontaneously without surgical therapy, whereas tangential excision and skin grafting are necessary for a majority of DDB and DB treatment. Hence, inaccurate diagnosis might bring improper therapies, resulting in the abuse of medical resources in SDB treatment and the loss of perfect time to cure DDB. However, there are difficulties distinguishing SDB from DDB because of the small differences in destruction of papillary and reticular dermis. Clinically, diagnosis of burn depth mainly depends on visual observation or pin-prick tests [3], which are greatly limited by surgeons' experiences and usually inaccurate. Burn biopsy is considered as the gold standard of burn depth assessment. But multiple biopsies are commonly required because of inhomogeneous burn depth in different sites, which causes additional scars and more diagnostic time delay.

Many technologies have been developed to produce objective judgments so far, such as laser Doppler imaging (LDI) [4], polarization-sensitive optical coherence tomography (PSOCT) [5,6]. LDI detects blood flow that might be reduced or stopped within burn region. The velocity of blood flow is relative to burn depth, where upper skin layer has faster blood flow and the deeper is slower. LDI system enables noncontact, wide area measurements through mapping two-dimensional color-coded images of blood flow. However, the

correlation between depth of burns and blood flow is not straightforward, resulting in poor resolution for depth assessment. PSOCT can provide quantitative depth measurement of burn injury by cross-sectional imaging with high spatial resolution. It measures depth resolved optical polarization changes, caused by thermal damages of collagen, of reflected light from burn tissues. The PSOCT signal is closely related to tissue's optical scattering coefficient, which conversely restricts itself to a shallow imaging depth of about 1 mm because of strong light scattering. Therefore, a noninvasive and fast imaging system with accurate diagnosis is highly desirable to clinical burn depth evaluation.

Photoacoustic (PA) imaging is a hybrid *in vivo* imaging technique combined optical and ultrasound imaging. It acoustically detects light absorption in tissue based on the PA effect. Compared to optical scattering in tissue propagation, ultrasonic scattering is 2~3 orders of magnitude weaker, possessing deeper transmission ability of PA wave. PA imaging has two main implementations as PA computed tomography (PACT) and PA microscopy (PAM). Utilizing high energy pulsed laser and ultrasonic transducer array, PACT can achieve an imaging depth up to 4 centimeters maintaining a spatial resolution of 255 μm [7], which can be applied to investigate heart and brain diseases in macroscale [8,9]. PAM has a better lateral resolution of even less than 1 μm [10] by focusing laser beam and acoustic wave tightly but a lower imaging depth within millimeters. In microscale, PAM can be used to trace drug delivery in tumor microvessels [11,12]. Blood perfusion and neovascularization provide nutrients and remove waste in burn wound recovery. In particular, hemoglobin is a natural endogenous PA contrast agent in visible spectrum. Hence, PA imaging can realize structural and functional imaging of burn healing by detecting hemoglobin absorption. Several studies showed the potential application of PA imaging on detecting animal skin tissue changes induced by thermal injury. Real-time PACT was used to assess burn depth and visualize distribution of albumin in burn model *in vivo* [13–15] as well as monitor skin tissue regeneration [16]. In previous work, researches performed three-dimensional (3D) imaging of burn, but did not acquire functional information and measure burn volume changes. Acoustic-resolution PAM was used to image acute pig skin burn *ex vivo* [17]. However, microvessel changes in hyperemic ring were not observed during burn healing.
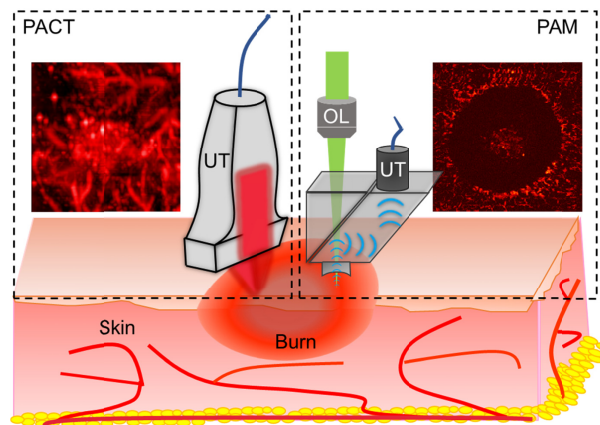

Fig. 1. Schematic of dual-scale photoacoustic imaging on skin burn injury. On the left is the PACT imaging model in dashed box and a representative PACT image of burn. On the right is the PAM imaging model and a PAM image of burn. UT, ultrasound transducer; OL, objective lens.

In this work, we intend to apply PACT and PAM together to realize dual-scale surveillance and assessment of two damage degrees of burn injuries (*i.e.* SDB and DDB) (Fig. 1). By volumetric imaging at multi-wavelength, PACT provided 3D structural and functional information of burn zone. In this way, we were able to analyze the differences of burn depths and oxygen saturation (sO_2) changes between SDB and DDB for accurate diagnosis. Besides,

we reconstructed 3D structures of burn region and quantified the volume changes during the burn healing process. Meanwhile, high-resolution images of angiogenesis on burn hyperemic ring were acquired through PAM imaging. The hyperemic ring is the boundary of thermal damage on skin surface. Imaging hyperemic ring would help better understand how burn heals. To the best of our knowledge, we for the first time employed dual-scale PA imaging on burn study in a long-term monitoring. Our method might provide new insights in burn diagnosis and healing mechanism study.

2. Methods

2.1 Animal preparation

All *in vivo* animal experimental procedures were approved by the Institutional Animal Care and Use Committee of Xiamen University. Male white mice (ICR, 20~22 g), bought from Xiamen University Laboratory Animal Center, were anesthetized using inhalation of 2% isoflurane to guarantee the entire procedure performed under anesthesia. The mouse hair in dorsal skin was firstly shaved and then depilated gently using hair removal creams. To avoid creams-induced chemical irritation on skin, the mice were raised normally for 24 h before burn modeling. Burn injuries were made on exposed dorsal skin by direct contact with an electric soldering iron thermostatically set to a temperature at 200°C, which is confirmed by a thermal temperature sensor (Ax5, FLIR). Mice were randomly divided into two groups and inflicted heating with 5 and 8 seconds duration, respectively, to model SDB and DDB injuries. To make different models, the burn areas were 10×6 mm^2 shaped in ellipse for PACT and 4 mm diameter round for PAM, respectively. Before imaging, ultrasonic gel was applied on skin and a customized water tank filled with deionized water was placed upon gel to optimize PA signals transmission efficiency. The bottom of water tank was a layer of transparent polyethylene membrane that allows laser beam and acoustic wave to travel through. While imaging, the mice limbs were fixed and kept still to avoid image artifacts brought by skin movement. A time point experiment was performed to investigate the PA signal changes of mouse skin healing after a burn injury. The healing process was completely natural without any ointments promotion.

2.2 PACT imaging

PACT images were collected using a commercial imaging system (Vevo LAZR-X, FUJIFILM VisualSonics Inc.) with a 40 MHz ultrasound array transducer (MX550D, FUJIFILM VisualSonics Inc.). When imaging, the ultrasound probe was immersed in water for acoustic coupling. The laser pulse was tunable in visible and near-infrared spectrum (680-970 nm and 1200-2000 nm), which was delivered through optical fiber bundles connected to both sides of ultrasound transducer and converged in front of transducer arrays. The operating laser wavelength was 680 nm in anatomical imaging for the reason that it was the shortest available wavelength with highest hemoglobin absorption. Meanwhile, 750/850 nm were selected in functional imaging because oxyhemoglobin (HbO$_2$) have higher absorption than deoxyhemoglobin (HbR) at 750 nm but HbR is dominant at 850 nm. The distinct molar extinction coefficients enable measuring the concentrations of HbO$_2$ and HbR to calculate sO$_2$ by the following equation [18]:

$$sO_2 = \frac{[HbO_2]}{[HbR]+[HbO_2]}. \tag{1}$$

The PACT imaging head was stabilized to a stepper motor to perform 3D volumetric imaging under a field of view (FOV) of 15×12 mm^2 with a step size of 0.1 mm, which generated about 150 frames images per scan. After that, multi-wavelength PA data were stored and reconstructed in VevoLab software (FUJIFILM VisualSonics Inc.) to display PA and sO$_2$ images. Here, every frame of 3D data presented cross-sectional view of skin tissue

and could be processed individually. Burn region was outlined for quantification by circling PA burn region of interest (ROI) in every frame and fitting all circles to generate 3D burn volume and calculate signal intensities.

2.3 PAM imaging

We built one laboratory high-resolution PAM to image the partial burn injury. Our PAM was characterized to have a lateral resolution of 10 μm at depth of 0.7 mm, which was enough to satisfy our imaging requirements. The laser wavelength is 532 nm with 7 ns pulse width (AONano532-1-40-V, Advanced Optowave Corporation), where hemoglobin has high molar extinction coefficient. A collimated laser beam was focused by a 4 × objective lens (RMS4X, Thorlabs) on skin surface, traveling through an optical-acoustic combiner designed to separate laser beam and acoustic wave. The incident laser pulse energy focused on sample surface is well within the American National Standards Institute safety limits [19]. The laser induced PA signals were then acquired by a 50-MHz central frequency ultrasound transducer (V214-BB-RM, Olympus) and digitized by a 14-bit data acquisition card (CSE1422, GaGe Applied Science). A raster scanning was performed to acquire data. Two-dimensional maximum-amplitude-projection (MAP) images were reconstructed by projecting maximum PA amplitude of each one-dimensional depth-resolved data. The reconstructed gray PAM images were processed and pseudo colored to enhance image contrast.

2.4 Histological examination

The mice were sacrificed after experiments. Then skin tissues containing burn injury were biopsied and sectioned. The sections were then fixed and stained with hematoxylin and eosin (H&E).

3. Results and discussion

As depth measurement is important in burn diagnosis, we first investigated the depth changes of mice burn healing process in SDB and DDB groups (n = 3, respectively). To evaluate depth values, cross-sectional PA images were acquired at pre-burn and post-burn 1, 2, 3, 4, 5, 7, 10, 14, 21 days (Fig. 2). Here, burn depths at each time point were calculated by measuring the PA-signal distance from skin surface to underlying layer as indicated by white double arrows in Figs. 2(a) and 2(c). The quantitative burn depth changes were plotted in Fig. 2(e). Before burn damage, the whole normal skin depths were 0.71 ± 0.01 mm and 0.54 ± 0.03 mm in SDB and DDB, respectively. When thermal damage occurred, the burn depth rose sharply and stayed high in both SDB and DDB. The difference was, in the first three days, the mean burn values of DDB depth (lowest, 1.68 ± 0.10 mm) were deeper than 1.6 mm while SDB (highest, 1.55 ± 0.15 mm) were lower than 1.6 mm. Therefore, the depth value of 1.6 mm could be a critical point distinguishing SDB from DDB [13]. The signals pointed by the yellow arrows came from the eschar of the skin surface. The more severe burn led to stronger PA signal since the light absorption of the eschar was much higher than that of hemoglobin. This could explain why PA signal intensity of skin surface, compared to that in SDB, was much higher in DDB in Fig. 2(c). As burn wound recovering, the burn depth started to decrease gradually from day 4. Hence, the depth diagnosis should be performed as early as possible in the first three days in case of inaccurate results. Since post-burn day 14, burn depth had turned down to a level as low as normal skin.

As for cross-sectional sO_2 images in Figs. 2(b) and 2(d), the burn depths also changed along with burning process. But the regularity was not as continuous as PA images showed, because sO_2 was changeable owing to blood perfusion. Therefore, the depth of sO_2 is unreliable to assess burn depth. The more important point conveyed in sO_2 images was that central area of burn had more hypoxia compared against surrounding area in first week. This was mainly caused by dermis damage lacking blood perfusion, especially in DDB. High magnification (100-fold) H&E histology images of skin tissues in SDB and DDB were

illustrated in Fig. 2(f), verifying the success in burn modeling. The white dashed lines indicate the boundary between burn and non-burn, which lies in papillary dermis in SDB while reticular dermis in DDB. The thickness of DDB was also thicker than SDB, confirming more severe thermal damage in DDB.
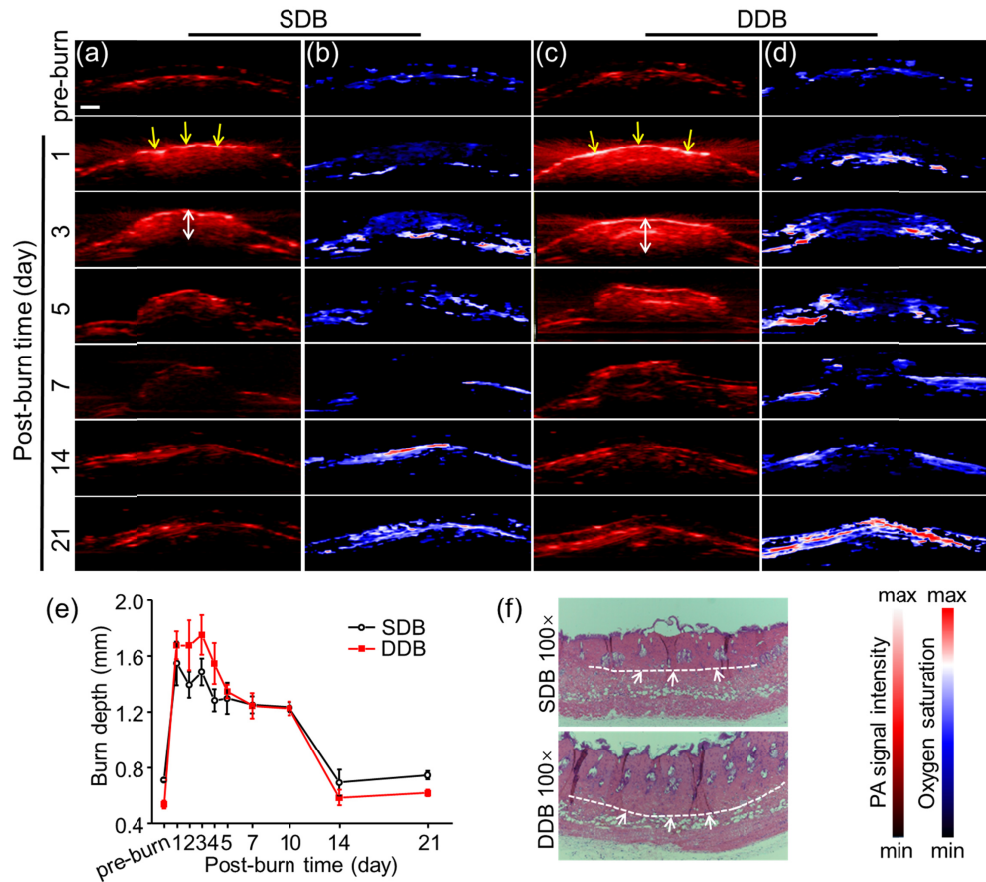

Fig. 2. Cross-sectional PACT images of burn injury. Cross-sectional PA structural images of (a) SDB and (c) DDB injuries are presented at selected time points. The yellow arrows indicate the eschar at skin surface after thermal damage. The white double arrows mark the burn depth of burn wound. Cross-sectional sO_2 images of (b) SDB and (d) DDB injuries are presented at selected time points. (e) Quantitative burn depth changes of two burn models in pre-burn and post-burn 21 days. DDB has deeper thermal damage than SDB. (f) H&E staining of skin tissues right after making SDB and DDB. Scale bar is 1 mm.

To study volumetric burn healing process, three-dimensional scanning was performed to image the entire burn region and obtain 3D PA structural and functional images (Fig. 3), after the procedure of cross-sectional PACT imaging. Reconstructed images of 3D burn area were shown in top-view with MAP rendering, providing overall observation. In Figs. 3(a) and 3(b), there are some similar tendencies in both SDB and DDB. Before burn damage, there were complete and numerous subcutaneous blood vessels in normal skin tissues. At post-burn day 1, the blood vessel signals disappeared and a large piece of signals emerged in the central FOV as indicated by yellow dashed circle. These signals were mainly composed of eschar and stasis of burn wound, which were very consistent with cross-sectional images in Figs. 2(a) and 2(c). However, compared with SDB, DDB image showed a brighter PA signal in central area on day 1 because of more severe thermal damage. Blood vessels regenerated at

day 3 and began to grow toward the center. At day 10, the faint circular signals in center are supposed from remaining red spot generated by sloughed eschar. After day 14, burn signals faded away and blood vessels were clearly shown. From normalized quantitative PA values of 3D burn region in Fig. 3(e), DDB reached the biggest value on day 1, which was much higher than SDB because of the strong absorption of eschar. The value of DDB then fell and rose to second peak and fell again eventually. SDB value rose linearly until day 4 and fell down after that, which was possibly caused by blood repair and diminished blood perfusion.
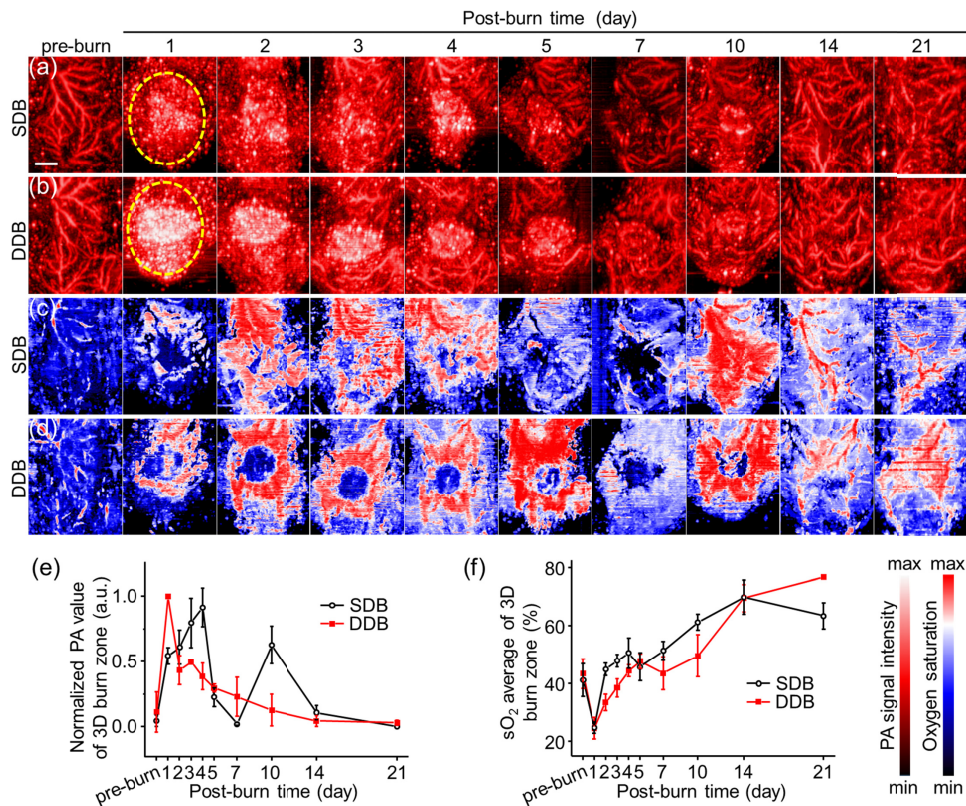

Fig. 3. 3D PACT imaging of burn injury at different days. Top-view PA images of (a) SDB and (b) DDB injuries. The burn region, indicated by yellow dashed circle, show strong PA signal due to optical absorption of eschar and stasis in early stage. (c) (d) Relative sO_2 images of (a) and (b). DDB has lower sO_2 in burn center because of suffering more severe thermal damage. Quantitative analysis of (e) volume photoacoustic signal amplitudes and (f) sO_2 averages of burn zone. Scale bar is 3 mm.

Figures 3(c) and 3(d) show the 3D sO_2 corresponding to Figs. 3(a) and 3(b), respectively. In DDB, there is an obvious hypoxia area in the central burn wound in Fig. 3(c), consistent with cross-sectional images in Fig. 2(d). The quantitative sO_2 average of burn region shows the difference between SDB and DDB in Fig. 3(f). SDB had a faster rate of ascent than DDB because DDB suffered more severe burn injury and had slower blood perfusion, resulting in slower sO_2 changes. The lower sO_2 of DDB can be used as a supplementary judgment to distinguish DDB from SDB. But it should be noticed that the sO_2 values were very close for both SDB and DDB on day 1, at ~24%. Therefore, the best time to detect sO_2 is on day 2 and day 3. The dividing value was supposed to be 40%, as SDB reached $44.9 \pm 2.2\%$ and $47.8 \pm 2.2\%$ while DDB reached $33.5 \pm 2.8\%$ and $38.6 \pm 3.1\%$ at day 2 and day 3, respectively. It can be deduced that measuring burn depth assessment and 3D sO_2 values together would bring a more accurate burn diagnosis at day 2 and day 3.

Burn region volume is another important indicator to assess healing process. To verify the hypothesis that burn volume declined linearly with burn healing, we investigated volume changes in burn injuries. After 3D PACT imaging, we were capable of measuring approximate burn region volumes. Burn region outline was drawn in the VevoLab via depicting the edge of burn wound frame by frame and shown in 3D meshes with surface rendering. After fitting, the software calculated out the approximate value of burn volume. Because normal skin tissues have no burn injury, Fig. 4 starts at day 1 without pre-burn volume. The reconstructed shape of burn area was an approximate ellipsoid, which was consistent with burn model made in Methods 2.1. The volume peak was not at day 1 but day 2, because tissue response to burn continued generally within 48 hours and volume reached a maximum at day 2. With burn healing, the volume shrank piece by piece to nearly none at day 21. Compared with DDB, SDB healed much better with smaller burn volume attributable to weaker thermal damage in skin tissue. This result is consistent with our assumption.
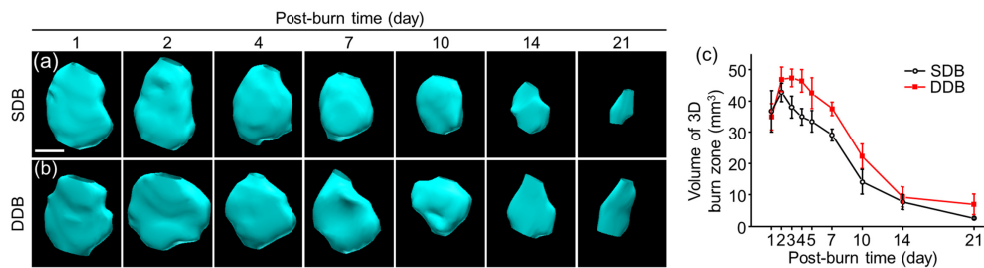

Fig. 4. Volume changes of burn injuries via time increases. Approximate 3D maps of reconstructed burn region of (a) SDB and (b) DDB. The elliptical shapes are well consistent with burn models. (c) Quantitative analysis of volume changes of SDB and DDB, where DDB has a larger volume due to more severe thermal damage. Scale bar is 2.5 mm.

Most of previous study focused on macroscale pathological changes about burn healing process. Here, we applied high-resolution PAM to image burn wound, especially hyperemic ring that defines the boundary of the thermal damage. Imaging on hyperemic ring would help understand the burn healing process better. Because we were more concerned about the changes of blood vessels and the results of SDB and DDB showed similar features in the hyperemic ring PAM images, we only presented the DDB results (Fig. 5). Figure 5(a) shows the PAM images of burn healing within 10 days. The bright discoidal signals in the first two days were skin surface eschar and faded away as time went by. PAM images illustrate clear micro-vessels growing in hyperemic ring, indicated by white arrows, during burn healing. The blood vessels in hyperemic ring emerged at day 2 and became more obvious. To quantitatively calculate the vessel densities, the vessel structures without central eschar signals were extracted through skeletonization algorithm [20], which matched well with the PAM images as Fig. 5 (b) showed the result of day 4. From Fig. 5(c), it could be seen that the blood vessel density rose to peak at day 4 and then fell with burn healing, showing a similar changing tendency in PACT. The denser blood vessels induced relatively high sO_2 in early stage as measured in PACT. The inner diameter of the hyperemic ring was calculated as well to quantify the shrinkage rate as shown in Fig. 5(d). The descent rate was in good agreement with the decreasing tendency measured in burn depth and volume changes in PACT, which remained high in the first three days and declined gradually with burn healing. The slow changes, in early stage, of either hyperemic ring shrinkage or burn region volume reduction indicated that skin tissue requires longer response time to rescue from acute burn injury.

The results acquired from PACT and PAM showed pathological changes of burn tissues from macroscale to microscale. In the recovery process, the depth and the volume of burn region detected by PACT as well as diameter of inner hyperemic ring detected by PAM decreased simultaneously. In the first four days, blood vessel density inside the hyperemic

ring increased showing the similar increment of sO_2 changes. However, after day 4 post-burn, the blood vessel density of hyperemic ring decreased but the sO_2 of whole burn region kept increasing. The different changing trends might be mainly caused by the regeneration of subcutaneous blood vessels. The sO_2 contributions from hyperemic had negligible influence on whole burn region.
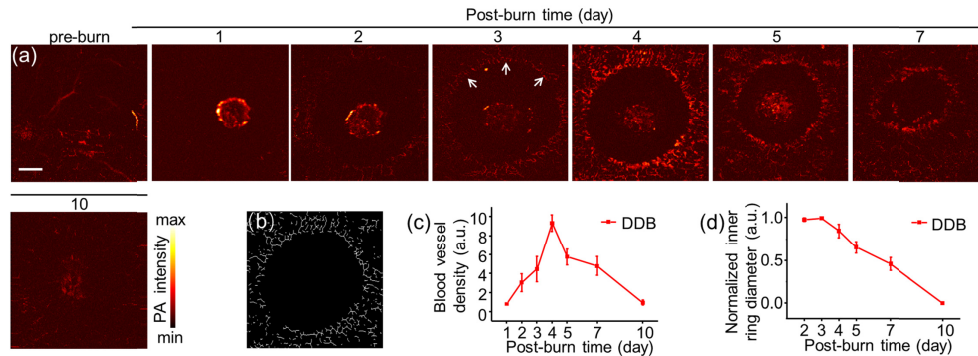

Fig. 5. PAM imaging of skin surface in burn injuries. (a) High-resolution PAM images of DDB at different time points. The blood vessel signals peak on day 4 and fade after 10 days. White arrows point to the hyperemic ring. (b) Representative vessel structure extracted through skeletonization algorithm at day 4. (c) Relative blood vessel density of (a). (d) Normalized inner diameter of hyperemic ring. Scale bar is 1 mm.

4. Conclusion

Burn depth assessment plays a vital role in burn diagnosis. By applying PACT, we were able to image burn injury in cross-sectional views to assess burn depths between SDB and DDB, and find the important milestone point, 1.6 mm, to distinguish DDB from SDB. Utilizing multi-wavelength laser pulses, we also performed structural and functional imaging on burn region. After thermal damage, the subcutaneous blood vessels disappeared and regenerated with burn healing. The recovering blood perfusion brings different sO_2 status. The DDB had more hypoxia and slower sO_2 changes than SDB due to more severe burn injury. A sO_2 value of 40% was supposed to separate DDB (lower than 40%) from SDB at post-burn day 2 and day 3. In addition, we visualized the burn volume changes by 3D reconstructing, which decreased generally as expected. To investigate the micro-vessel changes in hyperemic ring, we employed a high-resolution PAM to image burn wound. The PAM images show imperceptible angiogenesis with changes of blood vessel density and inner hyperemic ring diameter quantified.

In summary, we applied PACT and PAM together to monitor burn healing process in macroscale and microscale. To the best of our knowledge, dual-scale images of PA signal changes of skin burn injury were presented simultaneously to unveil the disease pathological status for the first time. The dual-scale PA imaging capability strengthens the potential applications on burn surveillance and assessment.

Funding

Disclosures

The authors declare that there are no conflicts of interest related to this article.

References

1. American Burn Association, "Burn Incidence and Treatment in the United States: 2016" *http://ameriburn.org/who-we-are/media/burn-incidence-fact-sheet/.*
2. K. Mattox, *Trauma* (McGraw-Hill Education, 2017).
3. B. S. Atiyeh, S. W. Gunn, and S. N. Hayek, "State of the art in burn treatment," World J. Surg. **29**(2), 131–148 (2005).
4. D. H. Park, J. W. Hwang, K. S. Jang, D. G. Han, K. Y. Ahn, and B. S. Baik, "Use of laser Doppler flowmetry for estimation of the depth of burns," Plast. Reconstr. Surg. **101**(6), 1516–1523 (1998).
5. S. M. Srinivas, J. F. de Boer, H. Park, K. Keikhanzadeh, H. E. L. Huang, J. Zhang, W. Q. Jung, Z. Chen, and J. S. Nelson, "Determination of burn depth by polarization-sensitive optical coherence tomography," J. Biomed. Opt. **9**(1), 207–212 (2004).
6. M. Todorović, S. Jiao, J. Ai, D. Pereda-Cubián, G. Stoica, and L. V. Wang, "In vivo burn imaging using Mueller optical coherence tomography," Opt. Express **16**(14), 10279–10284 (2008).
7. L. Lin, P. Hu, J. Shi, C. M. Appleton, K. Maslov, L. Li, R. Zhang, and L. V. Wang, "Single-breath-hold photoacoustic computed tomography of the breast," Nat. Commun. **9**(1), 2352 (2018).
8. W. Li, R. Chen, J. Lv, H. Wang, Y. Liu, Y. Peng, Z. Qian, G. Fu, and L. Nie, "In Vivo Photoacoustic Imaging of Brain Injury and Rehabilitation by High-Efficient Near-Infrared Dye Labeled Mesenchymal Stem Cells with Enhanced Brain Barrier Permeability," Adv. Sci. (Weinh.) **5**(2), 1700277 (2018).
9. J. Lv, Y. Peng, S. Li, Z. Guo, Q. Zhao, X. Zhang, and L. Nie, "Hemispherical photoacoustic imaging of myocardial infarction: in vivo detection and monitoring," Eur. Radiol. **28**(5), 2176–2183 (2018).
10. D. K. Yao, K. Maslov, K. K. Shung, Q. Zhou, and L. V. Wang, "In vivo label-free photoacoustic microscopy of cell nuclei by excitation of DNA and RNA," Opt. Lett. **35**(24), 4139–4141 (2010).
11. W. Li, X. Sun, Y. Wang, G. Niu, X. Chen, Z. Qian, and L. Nie, "In vivo quantitative photoacoustic microscopy of gold nanostar kinetics in mouse organs," Biomed. Opt. Express **5**(8), 2679–2685 (2014).
12. L. Nie, P. Huang, W. Li, X. Yan, A. Jin, Z. Wang, Y. Tang, S. Wang, X. Zhang, G. Niu, and X. Chen, "Early-stage imaging of nanocarrier-enhanced chemotherapy response in living subjects by scalable photoacoustic microscopy," ACS Nano **8**(12), 12141–12150 (2014).
13. T. Ida, Y. Kawaguchi, S. Kawauchi, K. Iwaya, H. Tsuda, D. Saitoh, S. Sato, and T. Iwai, "Real-time photoacoustic imaging system for burn diagnosis," J. Biomed. Opt. **19**(8), 086013 (2014).
14. M. Yamazaki, S. Sato, H. Ashida, D. Saito, Y. Okada, and M. Obara, "Measurement of burn depths in rats using multiwavelength photoacoustic depth profiling," J. Biomed. Opt. **10**(6), 064011 (2005).
15. Y. Tsunoi, S. Sato, S. Kawauchi, H. Ashida, D. Saitoh, and M. Terakawa, "In vivo photoacoustic molecular imaging of the distribution of serum albumin in rat burned skin," Burns **39**(7), 1403–1408 (2013).
16. S. Y. Nam, E. Chung, L. J. Suggs, and S. Y. Emelianov, "Combined ultrasound and photoacoustic imaging to noninvasively assess burn injury and selectively monitor a regenerative tissue-engineered construct," Tissue Eng. Part C Methods **21**(6), 557–566 (2015).
17. H. F. Zhang, K. Maslov, G. Stoica, and L. V. Wang, "Imaging acute thermal burns by photoacoustic microscopy," J. Biomed. Opt. **11**(5), 054033 (2006).
18. C. Li and L. V. Wang, "Photoacoustic tomography and sensing in biomedicine," Phys. Med. Biol. **54**(19), R59–R97 (2009).
19. American National Standards Institute, "American National Standard for Safe Use of Lasers," (ANSI, 2014).
20. K. M. Meiburger, S. Y. Nam, E. Chung, L. J. Suggs, S. Y. Emelianov, and F. Molinari, "Skeletonization algorithm-based blood vessel quantification using in vivo 3D photoacoustic imaging," Phys. Med. Biol. **61**(22), 7994–8009 (2016).